Suprathermal electron dynamics and MHD instabilities in a tokamak

J. Kamleitner[1], **S. Coda**[1], **J. Decker**[1], **J. P. Graves**[1]

[1] École Polytechnique Fédérale de Lausanne (EPFL) - Centre de Recherches en Physique des Plasmas (CRPP), CH-1015 Lausanne

E-mail: josef.kamleitner@alumni.tuwien.ac.at

Abstract. The dynamics of suprathermal electrons in the presence of magnetohydrodynamics (MHD) activity and the excitation of MHD modes by suprathermal electrons is studied experimentally to improve the understanding of the interaction of fast particles with MHD instabilities in a tokamak.
The study focuses on three different aspects of the internal kink mode with poloidal/toroidal mode number $m/n = 1/1$; the sawtooth instability, electron fishbones and coupled bursts alternating with sawtooth crashes (CAS), all located where the safety factor (q) profile approaches or takes values of $q = 1$.
New quantitative results on suprathermal electron transport and investigation of electron acceleration during sawtooth crashes are followed by the characterization of initial electron fishbone observations on the Tokamak à Configuration Variable (TCV). Finally, the CAS, whose $m/n = 1/1$ bursts are coupled to a background $m/n = 2/1$ mode and alternate with sawtooth crashes, are discussed, especially in view of the fast electron dynamics and their role in confinement degradation and mode excitation.

Keywords: Suprathermal electrons, MHD, hard X-ray, electron fishbones, sawtooth crash, internal kink mode

PACS numbers: 52.35.Py, 52.50.Sw, 52.55.Fa, 52.55.Tn, 52.55.Wq, 52.70.La

Submitted to: *Plasma Phys. Control. Fusion*

1. Introduction

Recent advances in suprathermal electron dynamics closely connected to magnetohydrodynamics (MHD) instabilities, especially the $m/n = 1/1$ internal kink mode, are presented. The experimental study on the Tokamak à Configuration Variable (TCV) [1, 2, 3] covers original results on fast electron acceleration and transport during sawtooth crashes, initial electron fishbone observations and mode coupling.

1.1. Sawtooth instability

The sawtooth instability is localized at the $q = 1$ surface, results in sawtooth-shaped core temperature time traces and can be partly explained by the Kadomtsev model [4, 5]. After a slow rise of central electron temperature ($T_{e,0}$), this model describes the evolution of an internal $m = 1$ kink mode leading to magnetic reconnection; this in turn results in enhanced bulk plasma transport during this so-called sawtooth crash and flattens the temperature profile. However, the predicted sawtooth period is not consistent with experiments and partial reconnection has been observed too [6].
Especially the magnetic reconnection process is not fully understood. The initial Sweet-Parker model [7, 8] was modified by Petschek [9] by adding a pair of shocks to the diffusive layer [10, 11]. Recent advances were achieved by collisionless reconnection models (based on two-fluid or kinetic description) [12, 13].
The experimental study of magnetic reconnection in a tokamak is very limited by the temporal and spatial resolution of diagnostics that can access the reconnection site. The investigation of particle acceleration by magnetic reconnection, for which several models for direct and stochastic acceleration exist [14, 15, 16, 17, 18], may be one of the keys to a fundamental understanding of the sawtooth instability and possibly to a mitigation of its negative effects, such as a reduction of energy and particle confinement and the triggering of secondary deleterious instabilities such as neoclassical tearing modes (NTMs) [19].
Indeed, the observation of electron acceleration during reconnection processes in sawtooth crashes (and disruptions) was reported for T-10 (hard X-ray (HXR) measurements) [20, 21] and TCV (electron cyclotron emission (ECE) diagnostics) [22]. The transport of suprathermal electrons by sawtooth crashes was studied in Tore Supra [23]. On TCV a large variety of sawteeth can be observed [24]; after the installation of the novel hard X-ray tomographic spectrometer (HXRS) [25, 26], a combined study of suprathermal electron transport and acceleration during sawtooth crashes is presented here in section 3.

1.2. Electron fishbones

Fast ions can excite MHD instabilities near the $q = 1$ surface, that are, due to the characteristic bursty (and frequency chirping) signal on the Mirnov coils, called "fishbones". This phenomenon was first observed in the PDX tokamak during neutral beam heating (NBH), causing a $20 - 40\%$ loss of beam heating power [27]. The result was also confirmed and studied on other tokamak experiments like JET [28, 29, 30]. The mode is identified as a $m/n = 1/1$ internal kink whose excitation can be explained by the resonant interaction of fast ions at the diamagnetic velocity corresponding to the phase velocity of the mode [31, 32].
Recently, similar modes were observed under conditions without ions fulfilling the resonance condition, but under the presence of strong electron cyclotron resonant heating (ECRH) and/or lower hybrid current drive (LHCD). Therefore, it is proposed that fast electrons excite these "electron fishbones". The first observation was reported from DIII-D during off-axis electron cyclotron current drive (ECCD) with the resonance layer on the high field side (HFS), close to the $q_{\min} \gtrsim 1$ surface, and NBH [33]; it represents the only observation in non-circular plasmas so far.
On HL-1M the mode occurred during ECRH on the HFS near the $q = 1$ surface. Additional LHCD enhanced the mode but could not drive it alone [34]. At much higher power, LHCD alone lead to the fishbone instability on Frascati Tokamak Upgrade (FTU), where the redistribution of suprathermal electrons due to the mode is claimed to be observed too [35]. On HL-2A, where fishbone-like modes were not only seen during HFS, but also low field side (LFS) ECRH deposition at the $q = 1$ surface, the mode excitation resonance condition was investigated in more detail; including HXR measurements and a comparison to ion fishbones [36, 37, 29]. Observations during LHCD discharges [38] on Tore Supra [39] were compared to the FTU results in [40]. Finally, fishbone-like modes during LHCD are also reported from Alcator C-Mod [41].

Up to now there is no complete picture of the electron fishbone instability; according to the current understanding it occurs close to the $q = 1$ surface, preferentially with low or reversed central shear, even with $q_{\min}$ being slightly above unity [42]. There are no sawteeth in the latter case [33, 40], whereas fishbone bursts alternate with sawteeth in discharges with $q < 1$ [34, 35, 41]. In any case, the drift reversal of the precessing fast electrons driving the mode depends significantly on the local magnetic shear, also via the impact on penetration of shaping [42]. The required inverted spatial gradient of fast electrons is usually accompanied by hollow central electron pressure (p_e) profiles. In terms of plasma shape, circular plasmas are more prone to the instability than elongated plasmas [42]. While barely passing electrons may also resonate with the mode, the role of freely passing particles seems to be limited to the regulation of the pressure and current profiles [43].
The change of the radial position of the mode during a burst can be attributed to the evolution of the equilibrium (q-profile) [40]. The characteristic frequency chirping is connected to the evolution of the resonant electrons' energy and subsequent change in resonant condition. This is also accompanied by a radial displacement of the mode and is reproduced in simulations [44].
The main relevance of electron fishbone studies lies in their parallels to ion fishbones in future burning fusion plasmas with significant alpha particle (α) heating; mainly because large fractions of the particle species are suprathermal, but still in small orbits. Moreover, electron heating systems allow for greater flexibility. As compared to the most advanced fast ion diagnostics such as neutron detectors [45], suprathermal electron diagnostics provide a much better spatial, energy and time resolution, to analyze the excitation model quantitatively, including the importance of the different regions in velocity space (barely/deeply trapped/passing), and on TCV also with respect to plasma shaping.
Despite the good qualitative description theory provides [43, 40, 46, 42], there are apparent differences in the observations on the various tokamaks. A more systematic experimental study may strongly advance the qualitative description and possibly allow a quantitative description of the electron fishbone mode. Such a study is performed on TCV, where a unique combination of high-resolution MHD and suprathermal electron diagnostics together with high power ECRH is available; the first results are presented in section 4.

1.3. Mode coupling

Mode coupling plays an important role in the fast seeding of NTMs by sawtooth crashes [19] and is one of the main reasons why sawtooth-free advanced scenarios are seen favorable for large tokamaks like ITER [47]. The theory of coupling of helical (m, n) harmonics to $(m \pm 1, n)$ sidebands was recently advanced [48] by an extension of the "resistive infernal mode" model [49] and underlined by extended MHD simulations of infernal-to-tearing mode coupling [50].
Section 5 presents the dynamics of the bursty mode, or coupled bursts alternating with sawtooth crashes (CAS), where the bursts are $m = 1$ and alternating with sawteeth while an $m = 2$ background mode persists. The evolution of the CAS is closely connected to the EC-heated suprathermal electron population at the $q = 1$ surface.

2. Experimental conditions, tools and methods

2.1. TCV tokamak

TCV is a conventional aspect ratio tokamak (major radius (R) 0.88 m, minor radius (a) 0.25 m) and a major European fusion facility [1, 2, 3]. TCV provides unique plasma shaping capabilities and covers a large range of plasma parameters. It features an extremely high power density ECRH and ECCD system, which is also highly flexible due to 6 independently real-time controllable 2nd harmonic extraordinary mode (X-mode) (X2) launchers [51, 52]. During the presented experiments up to 5 gyrotrons (launchers) with a total power of 2.5 MW were ready to tailor the current profile and electron distribution function (e.d.f.) appropriately.
Together with the state of the art diagnostic systems presented in the following, TCV therefore is an optimal environment for suprathermal electron and MHD studies [26, 53, 54].

2.2. MHD diagnostics

The duplex multiwire proportional X-ray counter (DMPX) diagnostic detects soft X-ray (SXR) radiation in two energy bins ($2 - 30$ keV in top and $4 - 30$ keV in bottom chamber) at high spatial (7.9 mm and 16.3 mm chord spacing) and temporal resolution (50 kHz, acquisition at 250 kHz) [55]; it is the main diagnostic for sawtooth detection and analysis on TCV.
The soft X-ray tomography (XTOMO) comprises 10 SXR cameras with 20 lines of sight (LoS) each, acquired at 100 kHz [56, 57]. In conjunction with the general tomographic inversion (GTI) code [58] and its included singular value decomposition (SVD) analysis [59, 60, 61] MHD modes can be identified and quantified.
The magnetic probes, also called $\dot{B}$ probes or Mirnov coils, measure the change of the poloidal magnetic field (B_θ) component tangential to the vacuum vessel. TCV features 4 poloidal arrays with 38 and 3 toroidal arrays

with 16+1 such pick-up coils each. Acquired at 250 kHz they provide data for toroidal (and poloidal) mode numbers up to 16 [62].

2.3. HXR diagnostics

The tangential X-Ray detector array (TXDA) measures HXR photon flux ($2-200$ keV) using cadmium-telluride ($CdTe$) detectors at typically 100 kHz. It was developed in conjunction with T-10, where a similar diagnostic is installed [63, 64]. A photo multiplier tube for hard-X rays (PMTX) monitors uncollimated MeV-range radiation escaping the TCV vacuum vessel.
The HXRS is the main HXR diagnostic at TCV, in the final design this tomographic system will consist of 4 cameras with 24 LoS each covering the whole poloidal cross section, resulting in a space resolution of a few cm. For the present studies the first 3 (LFS midplane, top, bottom) cameras were successively available and represent the key experimental instrument for suprathermal electrons. The present LFS camera can be rotated by 90 deg providing toroidal coverage in the co- and counter-current directions. [25, 65]
The detectors are $CdTe$ diodes with a system energy resolution of 7 keV covering a primary range from 13 to 300 keV. The full-pulse digital data acquisition, at 12 $\mathrm{M}^{\mathrm{samples}}/\mathrm{s}$, followed by digital post-processing, provides the time and energy of every single measured photon, allowing for data analysis based on arbitrarily chosen energy bins and time resolution. The latter depends on the photon statistics, with the detection system capable of handling up to 500 000 counts per second (cps) [66]. The statistics can be increased by conditional averaging with respect to (w.r.t.) sawtooth crashes or mode oscillation, increasing the effective time resolution from typically 10 ms to 0.1 ms or 10 μs, respectively.

3. Suprathermal electron dynamics during sawtooth crashes

The dynamics of the e.d.f. during sawtooth crashes, especially regarding transport and acceleration of suprathermal electrons, are studied in EC-heated low confinement mode (L-mode) plasmas in TCV. ECRH/CD is neither used for sawtooth triggering nor to stabilize sawteeth, such as to produce extremely long or large sawteeth (monster sawteeth). The sawtooth period is about $3-4$ ms and the crash amplitude is about $20-30\,\%$ in the SXR signal and in the bulk electron temperature relative to the peak before the crash. The HXRS can resolve the dynamics with 0.1 ms resolution due to conditional averaging w.r.t. the crash time. In a discharge typically a few hundred sawtooth crashes are detected by the DMPX and the reference time is put at the middle of the drop.

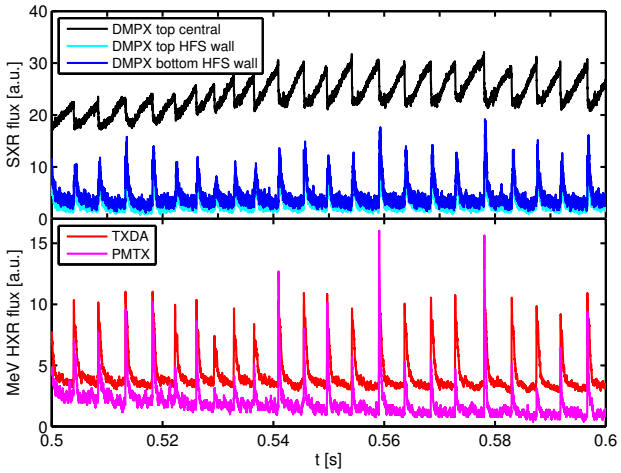

Figure 1. SXR DMPX signal and MeV HXR bursts (TXDA, PMTX) at sawtooth crashes in the low n_e TCV discharge 43039 ($P_{\mathrm{RF}} = 641$ kW, $n_{\mathrm{e,avg}} \approx 1.2 \cdot 10^{19}\,\mathrm{m}^{-3}$).

It turns out that two main regimes, primarily depending on electron density (n_e) and loop voltage (V_{loop}), can be distinguished. At higher density, the temporal variation of the HXR emission, and partially of suprathermal electron temperature ($T_{e,2}$), mimic those of the SXR and thermal bulk temperature. At low density, at the limit to a fully runaway discharge, HXR bursts in the MeV-range are observed immediately after each sawtooth crash.
The characteristics of these two regimes are presented below, followed by the even more interesting dynamics occurring in the transition region in between.

3.1. High density limit and low density cases

In medium and high electron density discharges, typically at $n_e \approx 3 \cdot 10^{19}\,\mathrm{m}^{-3}$ and above (high density limit), the temperature of the suprathermal tail is usually quite low, and so are the HXRS count rates above $E_\gamma \gtrsim 40$ keV; the presence of runaway electrons in particular can be excluded. In these discharges, the time evolution of the HXR and SXR emission is very similar and follows the typical sawtooth cycle of slow central emission rise followed by a sudden drop. The same behavior is also observed in the deduced temperatures for the bulk (T_e) and the suprathermal tail ($T_{e,2}$), with the only apparent difference that the relative temperature variation of the suprathermal tail is much lower than that of the bulk plasma, i.e. the suprathermal electron loss does not depend significantly on energy in the observed range $15-40$ keV.
While in the SXR and electron temperature (T_e) profiles a central flattening and radial broadening is observed, the suprathermal tail is reduced everywhere in temperature and density. Therefore no bulk

acceleration of electrons due to magnetic reconnection at the $q = 1$ surface can be inferred from HXRS data, while acceleration of electrons at thermal energies and/or at a lower rate as compared to the loss is not excluded.

At low electron density, typically $n_e \approx 1 \cdot 10^{19}\,\mathrm{m}^{-3}$, HXR bursts are observed by the TXDA and PMTX diagnostics (figure 1). In order to be detected by the PMTX their energy has to lie in the MeV-range. The shielding of the TXDA is insufficient for such energetic photons. Furthermore, a series of experiments with the TXDA tangentially observing different locations in the plasma, and in co- and counter-current direction, do not show any dependence of the measurement on either the location or the direction. This means that not even a distinguishable fraction of the TXDA signal comes from collimated radiation.
While the PMTX observes significant radiation outside of the bursts only in an initial phase of the discharge where it is fully runaway, the TXDA still collects reduced, but definitely non-zero radiation, attributed to a lowered, but persisting runaway electron population.
Also the blind HXRS detectors, especially in the lateral camera, see a finite number of high-energy photons in between the sawtooth crashes, while their signal is entirely saturated during the MeV gamma ray (γ) bursts coinciding with the crash. Therefore, the HXRS can detect these bursts and their duration, but cannot deliver any additional information such as emission location, photon flux or time evolution.
Due to its position in a bottom port and low detection efficiency (η) at high $E_\gamma > 30\,\mathrm{keV}$, the top DMPX camera signal is hardly affected by the bursty emission, only the bottom camera sees the bursts at the sawtooth crashes on all channels because of its thicker filter and therefore relatively increased η at higher energy. Interestingly, in both chambers the burst signal is largest in the channel looking at the HFS limiter. This indicates that high energy electrons hit the wall right after the sawtooth crash.
A possible explanation is that electrons are accelerated due to magnetic reconnection during the sawtooth crash and a part is also transported to the HFS wall. In this acceleration-dominated case significant high-energy bremsstrahlung emission comes from accelerated electrons remaining in the plasma. The alternative explanation is that the few persisting runaway electrons that are present in the plasma core emit little bremsstrahlung radiation due to their low collisionality there. During the sawtooth crash they are transported to the limiting wall, where they collide with the thick target.
Without spatial resolution or additional diagnostics (e.g. synchrotron radiation measurements of runaway electrons), the relative importance of these two effects cannot be quantified.

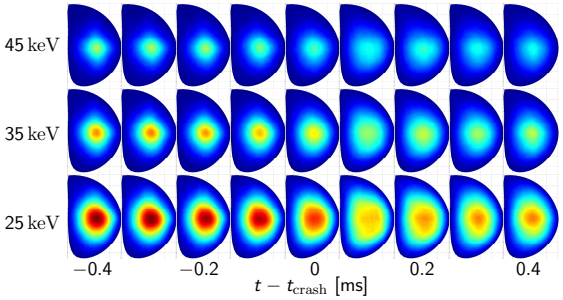

Figure 2. Evolution of the 2D HXR emission profile at different photon energies during a sawtooth crash in discharge 48228, obtained with GTI from conditionally averaged HXRS data of cameras 2 and 5.

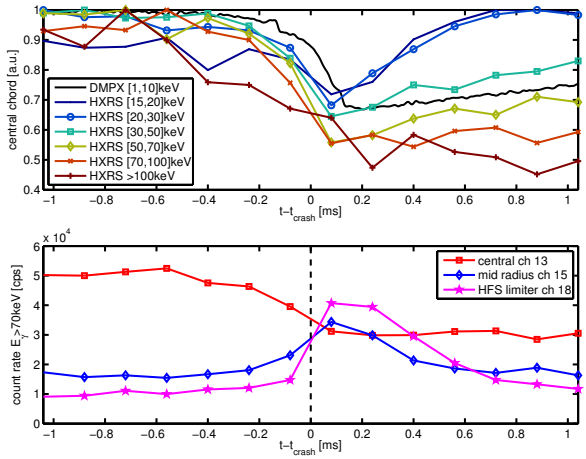

Figure 3. Evolution of the HXRS central chord measurement at different energies compared to the SXR evolution (top) and evolution of high energy HXR measurement from central, mid-radius and HFS limiter position (bottom) during a sawtooth crash in discharge 48228, obtained from conditional averaging.

3.2. Electron transport

The intermediate regime between the cases presented above is realized for instance in discharge 48228, at low density with significant current drive. That is, a high energy suprathermal tail is built up, but due to the low V_{loop} no runaways are present, confirmed by the blind detector of the upper HXRS camera 2. The lateral camera 5, being slightly perturbed by low level uncollimated HXR, can still be used in the lower energy bins where the radiation is collimated as in camera 2.
The result of the 2D tomographic inversion in the plasma center shows that the behavior there is similar to the higher density case with greatly increased suprathermal electron temperature and density; additionally, a broadening of the emission profile is observed (figure 2). The emission drop in the plasma core

is observed by the DMPX and HXRS central chords in different energy bins (figure 3), that show essentially the same evolution during the crash. After the crash, the low-energy HXR emission rises more rapidly than the SXR and high-energy HXR signals. This indicates that the suprathermal tail is built up rapidly at low energy and then grows to higher energy more slowly on the timescale of the T_e rise.

The chords of camera 2 that observe the HFS limiter register only a very low signal in the inter-crash phase. Right after the crash, however, the emission at high energies ($\gg 50\,\mathrm{keV}$) shows a burst with similar evolution as the bursts in the low density case, but at lower, still measurable energies, and collimated. The comparison to the central and a mid-radius chord (figure 3) shows that while the high energy HXR emission decreases in the center during the crash it already increases at mid-radius; 0.1 ms later, in the middle of the crash, the emission from the limiter increases much more quickly. The bottom of the central emission coincides with the top of the mid-radius and edge emission peak.

In summary, the central suprathermal electron distribution is significantly affected by sawtooth crashes throughout all energies observed, up to $\gtrsim 100\,\mathrm{keV}$. While the radial outwards suprathermal electron transport can be followed on the individual chords until a large fraction of the fast electrons hits the limiter and emits energetic HXR bursts, a contribution from acceleration could not be distinguished from the perpendicular HXR observation.

3.3. Electron acceleration

To investigate possible forward electron acceleration during the sawtooth crash at the high electron energies involved, tangential observation of the HXR emission is more efficient. With the HXRS camera 5, such measurements are performed for co-current ECCD (co-ECCD) (discharge 43205) and counter-current ECCD (cnt-ECCD) (43206). There, a change in MHD and sawtooth activity (longer period, larger crash amplitude) causes a density drop in the second phase of the discharge that puts it into the right parameter range for the intermediate regime.

As shown in figure 4 for co-ECCD and figure 5 for cnt-ECCD, the impact of the sawtooth crash is severe in both cases: the parallel HXR emission from the plasma center in the lower energy range ($20-50\,\mathrm{keV}$) drops to about one fourth within about 0.2 ms. At higher energies ($\approx 75\,\mathrm{keV}$), it falls only to a half. Energies above 100 keV are even less affected, which is also reflected in the increase of T_γ during the crash. The lower statistics prevent a precise quantification at such high energy.

The signal on the chords observing the HFS wall nearly tangentially and crossing the plasma center at an angle of about 45 deg drops also significantly at the crash in

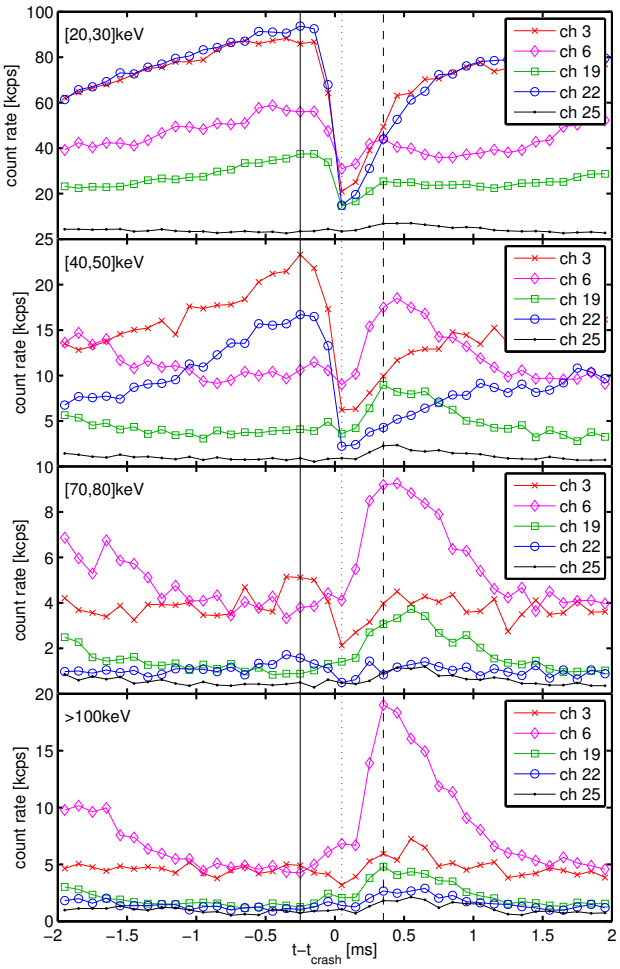

Figure 4. Time evolution of the HXR count rate in the tangential chords 3 (co-I_p view on plasma center), 6 (co-view on HFS wall), 19 (counter-I_p view on HFS wall), 22 (cnt-view on plasma center) and 25 (blind detector; background) in the co-ECCD discharge 43205.

the low energy range ($20-30\,\mathrm{keV}$), but hardly changes for $E_\gamma > 40\,\mathrm{keV}$. Interestingly, the relative drop depends, for all channel pairs, neither on the viewing nor on the current drive direction. This indicates a general suprathermal electron loss, probably depending on (parallel) momentum, during the sawtooth crash; in this phase, no signs of particle acceleration can be found in the HXR emission.

Immediately after the crash the HXRS suggests more complex dynamics. In the co-ECCD case the forward emission at $E_\gamma > 40\,\mathrm{keV}$ rises about twice as fast (0.4 ms) as the backward emission (0.8 ms) to a more than doubled emission. For cnt-ECCD this reheating is nearly equally fast in both directions (0.6 ms).

The co-view chord observing the HFS wall sees a quickly (0.2 ms) rising HXR burst at high energy, subsequently decaying with a time constant of about

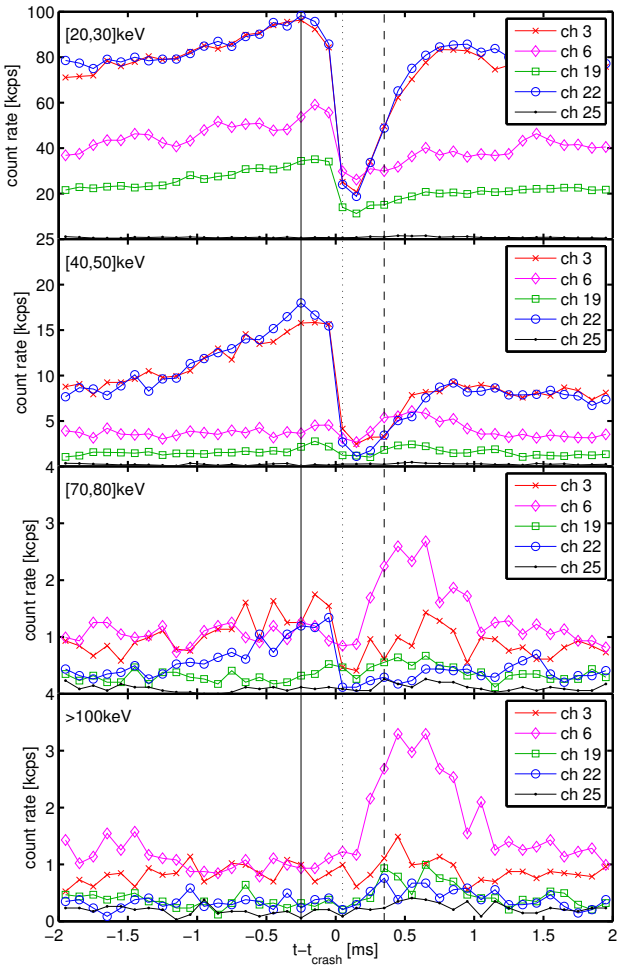

Figure 5. Time evolution of the HXR count rate in the tangential chords 3 (co-I_p view on plasma center), 6 (co-view on HFS wall), 19 (counter-I_p view on HFS wall), 22 (cnt-view on plasma center) and 25 (blind detector; background) in the cnt-ECCD discharge 43206.

0.6 ms. It is more intense for co-ECCD, where it is also observed by the cnt-view chord, at lower amplitude and energy.

There are only two intermediate chords and they do not cover the mid-radius position whose emission in discharge 48228 clearly indicates transport. But the time scales agree, the transport to the limiter occurs within 0.2 ms, i.e. at $\gtrsim 1.2\,^{km}/_{s}$. The slight time shift in energy hints that it may be on the slower side for electrons with higher parallel velocity ($v_\parallel$).

In contrast to the crash phase, now particle acceleration also seems to play a role: the emission above 100 keV rises beyond the pre-crash value in the chords observing the plasma center. Due to the low statistics, however, the acceleration cannot be quantified, but one observes that the accelerated particles are also quickly lost.

3.4. Discussion

Results on LHCD-created suprathermal tails at higher energy in giant sawteeth [23] suggest that electrons with relativistic $v_\parallel$ are hardly affected by sawtooth crashes. Due to larger perpendicular velocity ($v_\perp$) in the case of ECCD, neoclassical effects play a larger role than in the case of LHCD and may explain why suprathermal electron loss is still observed at energies around 100 keV on TCV. Also there are very significant differences, e.g. shaping, between the TCV and Tore Supra scenarios, prohibiting a quantitative comparison.

The distinction of the dominating suprathermal electron transport from electron acceleration is difficult, even with state-of-the art diagnostics; not only high resolution, but also excluding the misinterpretation of uncollimated photons as collimated measurement is essential. Nonetheless, the observed electron acceleration in T-10 [20, 21] could also be explained by significantly different plasma parameters favoring acceleration over transport.

While the observed energetic electron showers on the first wall should be mitigated by the high density in reactor-relevant conditions, anomalous transport of EC-heated suprathermal electrons by MHD activity may generally cause a reduced efficiency of ECRH and ECCD applications.

4. Electron fishbones

The electron fishbone experiments in TCV were developed from observations on other tokamaks and based on the existing theory (section 1.2). Accordingly, the main focus was on circular plasmas, in order to maximize the population of barely trapped electrons and the depth of their drift reversal. The therefore also pursued low-elongation (κ) negative-triangularity (δ) shape scenario had to be abandoned due to limited experimental time. X2 heating is localized on the HFS in a co-ECCD configuration, with the minor radius being scanned in toroidal magnetic field (B_ϕ) steps from shot to shot. This yields the required off-axis peaked pressure profile and a flat or slightly reversed q-profile due to co-ECCD and optional additional central cnt-ECCD.

The minimal q ($q_{\min}$) is ramped from above one through $q_{\min} = 1$ to below one and back by ramping the plasma current (I_p). The appearance of sawteeth indicates that the safety factor has dropped below one and compensates the lack of q-profile measurements in TCV. I_p has to be kept quite low due to the constraints in q and the rather low B_ϕ. The resulting T_e (ohmic preheating) is just sufficient for initial X2 absorption if n_e is comparably low. Such low n_e is also advantageous to increase the fraction of suprathermal

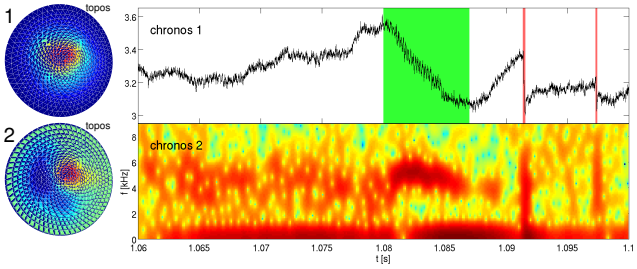

Figure 6. The first two XTOMO topos and chronos of TCV discharge 48440 showing the spatial structure in the poloidal plane (left), the time evolution of the amplitude in chronos 1 (top) and the frequency evolution in chronos 2 (bottom). The first chronos represents the background SXR emission profile and the second chronos the fishbone-like burst. The time interval of the burst appearance is indicated by a green area and the first two sawtooth crashes are highlighted by red areas in the first chronos plot.

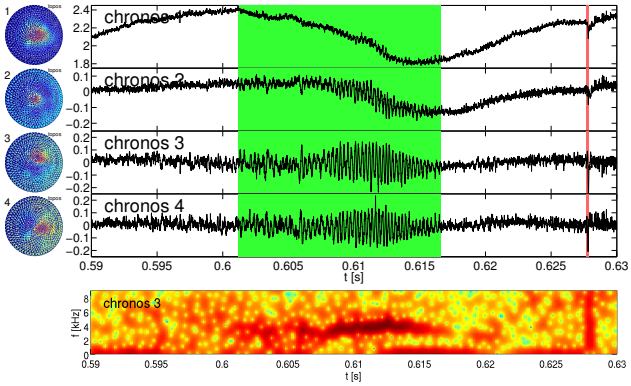

Figure 7. The first four XTOMO topos and chronos of TCV discharge 48442 showing the spatial structure in the poloidal plane (left), the time evolution of the amplitude (upper 4 plots) and the frequency evolution on the example of chronos 3 (bottom, same for chronos 4). The first chronos represents the background SXR emission profile and the pair of chronos 3 and 4 the fishbone-like burst. The time interval of the burst appearance is highlighted in green and the first sawteeth crash in red.

electrons, and subsequently the fraction of trapped energetic electrons.

The scenario is, due to this low n_e requirement, closely bounded by the threshold for significant runaway production and the threshold for good initial X2 absorption. The latter is the bigger concern, since X2 waves that are only partially absorbed and can thus escape the plasma may trigger the window protection system and shut down the gyrotrons; however, runaways are an issue for the HXRS and even SXR diagnostics signals (saturation).

In the presented experiments the HXRS is indeed partially saturated by uncollimated radiation originating from runaway electrons, whereas the XTOMO signals are not significantly perturbed; the tomographic inversion can be analyzed by SVD. This method identifies the main spatial and temporal structures (called topos and chronos, respectively) of a signal. It can be generally applied, not only on the time evolution of the 2D SXR emission profile in the poloidal plane, but for instance also on the magnetic probe signals.

4.1. Experimental observation

The first observation succeeds in TCV discharge 48440, with a slow I_p ramp (current ramp rate $dI_p/dt = 30\,\mathrm{kA/s}$) and constant n_e ($n_{e,0} = 2 \cdot 10^{19}\,\mathrm{m}^{-3}$). On the XTOMO, a single fishbone-like burst, a $m/n = 1/1$ mode chirping down in frequency, appears at $t = 1.08\,\mathrm{s}$ when $q_{\min} \approx 1$, just before the first sawtooth (figure 6). It is also observed by the LFS ECE system [67], but not by the magnetic probes.

In order to prolong the phase when the mode appears, 48440 was repeated at a constant $I_p = 164\,\mathrm{kA}$. In this discharge, 48442, a similar burst appears on the XTOMO (figure 7) and LFS-ECE, also just before the first sawtooth, when $q_{\min}$ drops below 1. Although the total current remains constant, $q_{\min}$ decreases due to the q-profile evolution. So the burst is not significantly longer than before. Again, it is not repeated, as had been observed on other tokamaks. In contrast to 48440, the frequency of the mode chirps upwards, which is unusual for electron fishbones.

Based on the very promising discharges 48440 and 48442, further discharges were performed in a later experimental session, aiming at lengthening the phase $q_{\min} \gtrapprox 1$ by slowly decreasing I_p. In theory, this should result in longer or even multiple bursts. Additionally, discharges with increased n_e were performed to prevent the generation of runaway electrons and obtain a useful HXRS measurement. However, none of these discharges showed any evidence of modes similar to those of 48440 and 48442. Moreover, even a straight repetition of 48442 in discharge 48717 could not reproduce the fishbone-like mode, although all plasma parameters (except 10 % different density) were well matched.

This hints that the discharge conditions are such that the mode is only marginally unstable. Therefore, a few more experiments based on 48440 were planned, but with modified heating and current profile tailoring, aimed at finding a more unstable point in parameter space. Due to the limited number of shots it was not possible to conduct all planned experiments and the ones that were performed did not contribute further fishbone-like observations.

4.2. Discussion

The oscillation in both successful TCV experiments is very similar, except for the direction of the frequency chirping. Experimental observations on

other tokamaks and theory tell us that electron fishbones chirp down in frequency because they are moving radially outwards and the temperature of the mode-driving electrons decreases.
In 48440 and 48442, however, the XTOMO shows that the radial extent of the mode shrinks slightly, by a few percent of poloidal flux surface label (ρ_{pol}). Since the Fokker-Planck simulation does not take any direct effects of the mode into account and there is no usable HXRS data, the evolution of the barely trapped (and passing) suprathermal electron population remains unclear. To be consistent with electron fishbone theory and observations on other tokamaks, the temperature of this population has to decrease in 48440, overcompensating the radial displacement, and increase in 48442. If the mode is not an electron fishbone, the differing frequency chirping direction could be explained by the different I_p and q-profile evolution.
In summary, the TCV experiments originated good candidates for electron fishbones. Lack of experimental data (HXRS polluted by runaways) and reproducibility prevent a definitive conclusion on the nature of the observed mode. Further investigation was limited by experimental time, but is to be continued in future campaigns at TCV.

5. Bursty mode (CAS)

The bursty mode, or coupled bursts alternating with sawtooth crashes (CAS), is often observed in EC-heated plasmas in TCV under certain conditions. Here two typical cases are presented, a first scenario with pure ECRH (figure 8) and a second scenario with an optimized ECCD deposition profile (figure 12) and increased mode amplitude. Generally, a $m/n = 2/1$ mode with changing amplitude persists in the background, while the main dynamics are characterized by regularly repeated $m/n = 1/1$ bursts that alternate with sawtooth crashes. Being separated in time, the bursts are neither a pre- nor a post-cursor of the crashes, but still closely connected.
A complete study has to cover dynamics at the burst occurrence rate as well as at the burst mode frequency (f_{mode}). The required data analysis is briefly introduced here before the results are presented.
The main reference point on the slower timescale is the fast p_e rise before a burst. Conditional sampling of Thomson scattering (TS) [68, 69] data and conditional averaging of HXRS w.r.t. these time points reveal thermal bulk and suprathermal electron dynamics during the preceding sawtooth crash and the following burst evolution on a sub-ms timescale.
The dynamics during the mode oscillations in the burst can be studied by averaging XTOMO and HXRS

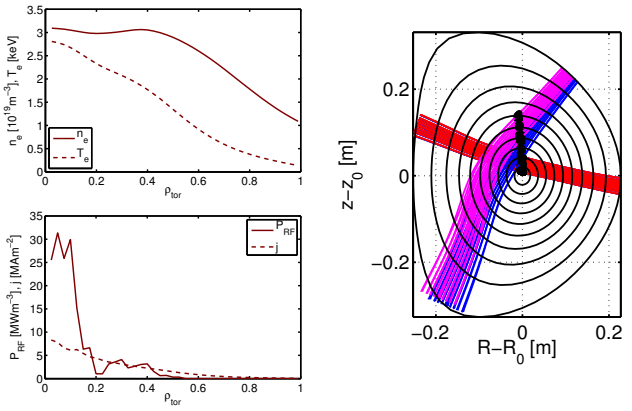

Figure 8. Density and T_e profiles (left), ray-tracing (middle) and RF absorption and current profiles in the bursty mode discharge 43618 with pure ECRH.

data at $f_{\mathrm{mode}} \approx 7\,\mathrm{kHz}$. The reference times are obtained from the peaks in the first chronos of the SVD corresponding to the frequency band filtered tomographically inverted XTOMO data, resulting in the same 100 kHz time resolution for both X-ray diagnostics.
Since non-axisymmetric structures in the plasma (the mode) are slower than such a high time resolution, the assumption of toroidal axisymmetry in the X-ray emission breaks down. Being no concern for the XTOMO, whose cameras are located in the same sector (#11) of TCV, the different toroidal location of the HXRS cameras (2 and 7 in sector 4, 5 in sector 9) has to be taken into account. For a toroidal mode number n the difference in toroidal angle ($\Delta\phi$) corresponds to a time shift

$$\Delta t = \sigma \frac{n\Delta\phi}{2\pi f}, \tag{1}$$

where f is the mode frequency (f_{mode}) and $\sigma \in \{\pm 1\}$ is a sign depending on helicity and rotation direction. The raw HXRS time traces of the individual cameras are time-shifted by Δt depending on their position w.r.t. sector 11 (XTOMO). Conditionally averaged, the HXR emission of $n = 0$ and $n = 1@f_{\mathrm{mode}}$ structures as if the HXRS cameras were all located in the XTOMO sector is reproduced. A standard tomographic inversion of this modified data then produces a correct result.

5.1. ECRH Scenario

In the triangular plasma ECRH scenario, central ECRH is applied with some additional off-axis heating (figure 8); mode bursts are observed on the SXR and MHD spectrograms.
On the XTOMO (figure 9), one or more sawtooth crashes are observed in the phases between the bursts of $\approx 2\,\mathrm{ms}$ length. A first sawtooth crash occurs $1-2\,\mathrm{ms}$

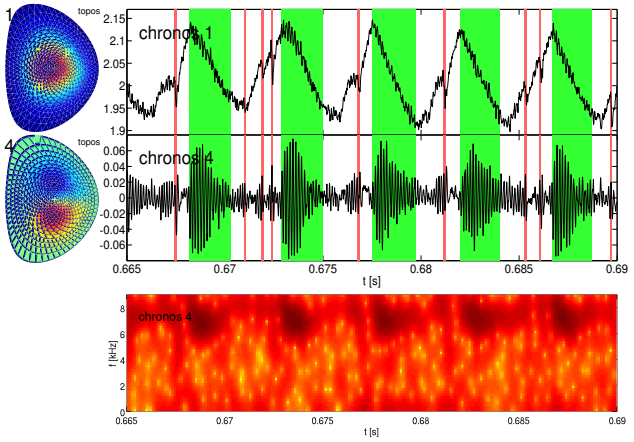

Figure 9. Evolution of the bursty mode in the scenario with pure ECRH: the main SXR emission is shown in topos and chronos 1 (top), and the $m = 1$ mode is represented by the topos-chronos pair 4 (middle). The red and green areas indicate sawtooth crashes and mode bursts, respectively. The spectrogram of chronos 4 (bottom) shows the frequency evolution of the mode.

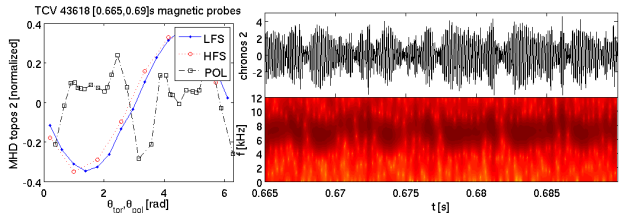

Figure 10. Bursty mode evolution in the SVD of the Mirnov coil (magnetic probe) arrays in scenario T.

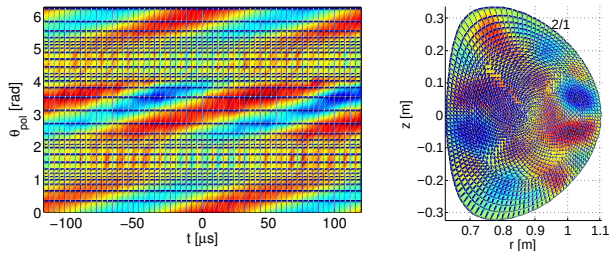

Figure 11. The evolution of one bursty mode period in the ECRH scenario on the poloidal Mirnov coil array (left), obtained with conditional averaging at time points from peak detection in SVD chronos from GTI XTOMO, shows the $m = 2$ component. The subtraction of $m = 1$ from the GTI XTOMO SVD topos (right) reveals this $m = 2$ component also in the SXR data.

after the mode burst vanishes; if it happens rather early more sawteeth can follow before the next burst phase, while a rather late sawtooth has more impact and is not followed by others before the mode recurs. After a single late sawtooth or the last sawtooth of a series, the central SXR emission rises to a value that is significantly higher than the top of the sawtooth cycle. During this rise, which lasts for less than 1 ms, no mode activity is observed in the SXR signal.

At a certain point, the $m/n = 1/1$ mode is destabilized and grows within one or two oscillations ($f \approx 7\,\mathrm{kHz}$) to its maximal amplitude. Its impact on confinement is traced in the now decreasing central SXR emission. The amplitude of the mode hardly changes in the first half of the burst (after its sudden rise), before it decreases, while the mode frequency remains constant for the entire burst duration (figure 9).

On the Mirnov coil arrays (figure 10), the SVD of the toroidal arrays observes a toroidal mode number $n = 1$, as expected for the $m = 1$ mode. The poloidal array, however, shows two peaks, therefore $m = 2$. While the frequency is equal, the time evolution also differs significantly from the XTOMO (SXR) observation: the $m/n = 2/1$ mode persists and its amplitude varies irregularly, not in periodic self-similar bursts.
Nevertheless, the two modes are closely related. Since the mode frequency is the same, one can perform conditional averaging of the poloidal Mirnov coil array based on the GTI XTOMO SVD chronos (figure 11). It shows again the observation of $m = 2$ by the poloidal probes and also means that the modes (or mode components) are in phase, even over multiple bursts.
To eliminate the dominant modes in each of the two diagnostics, we make use of the principle that a rotation of a poloidal signal by $\Delta\theta_{\mathrm{pol}} = \pi$ (half a turn) keeps the even m components unchanged, while the odd components are inverted. The sum of the poloidal Mirnov array and its rotation therefore removes the main $m = 2$ feature. Still, no $m = 1$ component is revealed: very likely its magnetic perturbation is well shielded due to the very central location of the mode. In contrast, the difference of the GTI XTOMO SVD topos to its half a turn rotated counterpart eliminates the $m = 1$ component and unfolds the further off-axis $m = 2$ mode structure in figure 11. Its SXR amplitude is clearly weaker due to the generally lower emission at its location as compared to the central $m = 1$ structure.

5.2. ECCD Scenario

In the ECCD scenario, with co-ECCD located close to the $q = 1$ surface (figure 12), the bursty mode occurs again (figure 13). It shows essentially the same time evolution and spatial structure, and the frequency is only slightly shifted upwards. However, the amplitude of the mode is greatly increased, leading to a drop of central SXR emission (confinement) of about 15 %. Also, the (absolute and relative) signal drop in the preceding sawtooth crashes is reduced.

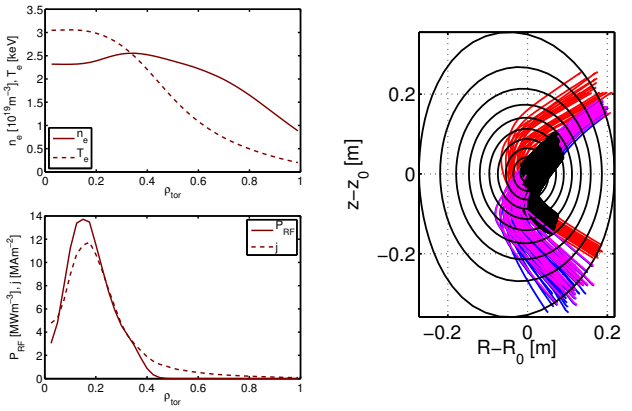

Figure 12. Density and T_e profiles (left), ray-tracing (middle) and RF absorption and current profiles in the bursty mode ECCD discharge 49315.

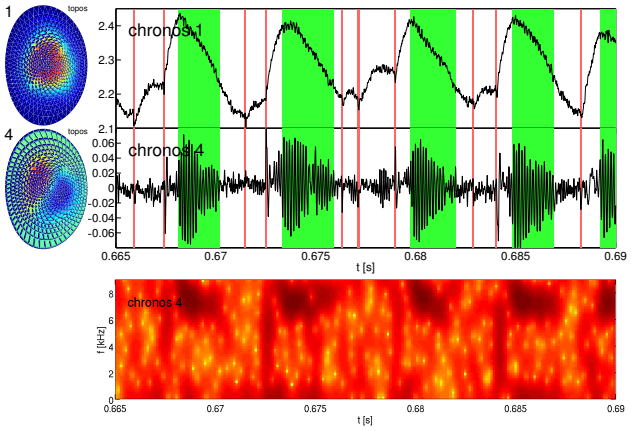

Figure 13. Evolution of the bursty mode in the scenario with slightly off-axis ECCD: the main SXR emission is shown in topos and chronos 1 (top), and the $m = 1$ mode is represented by the topos-chronos pair 4 (middle). The red and green areas indicate sawtooth crashes and mode bursts, respectively. The spectrogram of chronos 4 (bottom) shows the frequency evolution of the mode.

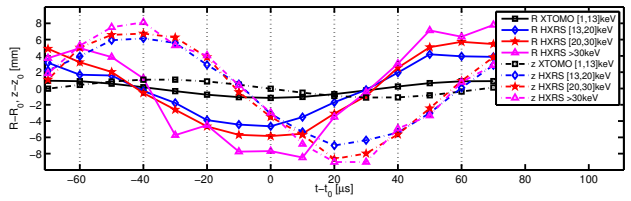

Figure 14. Evolution of the emission center (1st moment) in R and z direction during a mode period in discharge 49501; obtained from tomographic inversion of X-ray emission in the poloidal plane in 4 energy bins at several times in a mode period

5.3. Suprathermal electron dynamics during bursts

The effect of the fast $m/n = 1/1$ mode burst oscillations on the suprathermal tail is studied in discharge 49501. Having the same plasma parameters as the ECRH discharge 43618, 2D tomographic inversion of the HXRS is provided by the 3 cameras available (in 43618 only camera 5 was installed).
As shown in figure 14, the radial excursion of the first moment of the HXR emission pattern in the poloidal plane is much larger than in the SXR range, both exhibiting the $m/n = 1/1$ structure; an $m = 2$ component is not observed. The excursion in the HXR range increases further with photon energy (E_γ). In summary, the suprathermal electron population is significantly affected by the mode, and this is more pronounced at higher energies.

5.4. Mode excitation

The stability and excitation of the mode burst is studied with respect to the start of the p_e rise in the crucial phase after the last preceding sawtooth crash. Conditional averaging (and shifting) of TS data delivers n_e, T_e and subsequently p_e profiles (figure 15); their time evolution is additionally verified by a cross-check with tomographic inversion of far infrared interferometer (FIR) [70] and DMPX data. Similarly, the corresponding suprathermal electron pressure (p_{se}) profile can be estimated from HXR emission (figure 16). The mode evolution can then be explained in conjunction with the typical q profile evolution during sawtooth cycles.
The last burst-preceding sawtooth crash flattens the central q profile and increases $q_{\min}$. Suprathermal electrons are, as generally observed for sawtooth crashes, ejected from their slightly off-axis peaked location at the $q = 1$ surface. Meanwhile, $T_{e,2}$ and the thermal profiles do not change significantly.
After the expulsion of some of the suprathermal electrons, the suprathermal electron population grows rapidly and broadly in the whole plasma center, up to $\rho_{\rm tor} \approx 0.35$. As already observed for sawteeth in the intermediate regime (section 3.2), the suprathermal electron pressure rises more rapidly than its thermal counterpart during a phase in which the q profile is still flat in the center. While the insufficient T_e and the elevated $q_{\min}$ prolong the stability against a sawtooth crash, the suprathermal electrons, aided by the flat central $q \approx 1$, already destabilize the bursty mode. The importance of strong coupling to the present $m = 2$ component under these q profile conditions may also play a major role in the excitation of the $m = 1$ burst. Due to its impact on confinement, the mode then reduces $T_{e,0}$ and prevents sawtooth crashes during its whole duration. Since the mode mainly drags the

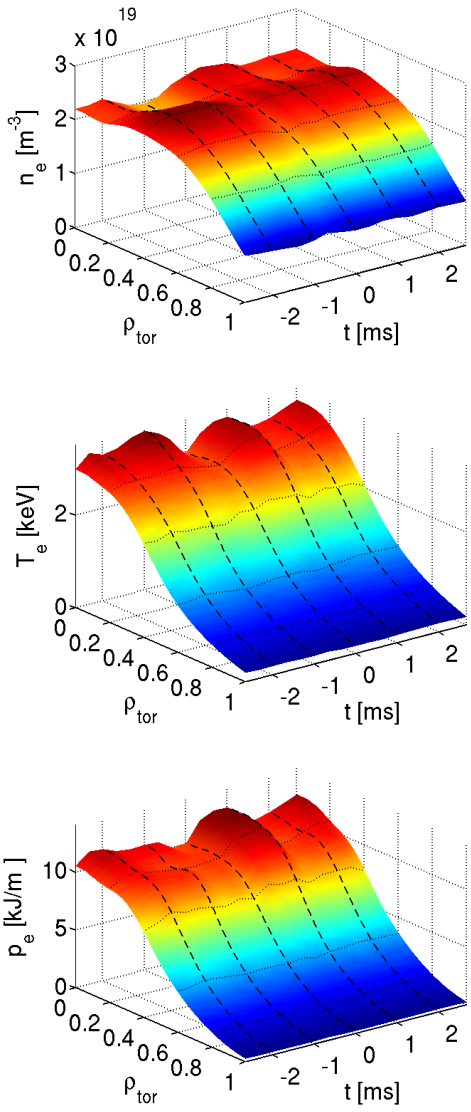

Figure 15. The evolution of n_e (top), T_e (middle) and p_e (bottom) measured by TS, conditionally averaged w.r.t. the start of the p_e rise ($t = 0$) after the last mode-preceding sawtooth crash ($t \approx 0.4\,\mathrm{ms}$); the mode burst occurs in $t = [0.2, 1.3]\,\mathrm{ms}$.

suprathermal electrons around, rather than ejecting them from its habitat, the mode persist. Ultimately, due to diffusion of the I_p profile, the central q drops again, reducing the mode drive and therefore its amplitude.

After the mode has diminished, $q_{\min}$ - by then significantly reduced - and the adequate present p_e destabilize a sawtooth crash. Especially crashes with small amplitude seem to be insufficient to produce the conditions required for a destabilization of the bursty mode, e.g. regarding the rise and flattening in q (possibly incomplete reconnection). Hence, they can be followed by one or more sawteeth, eventually re-establishing the bursty mode destabilization.

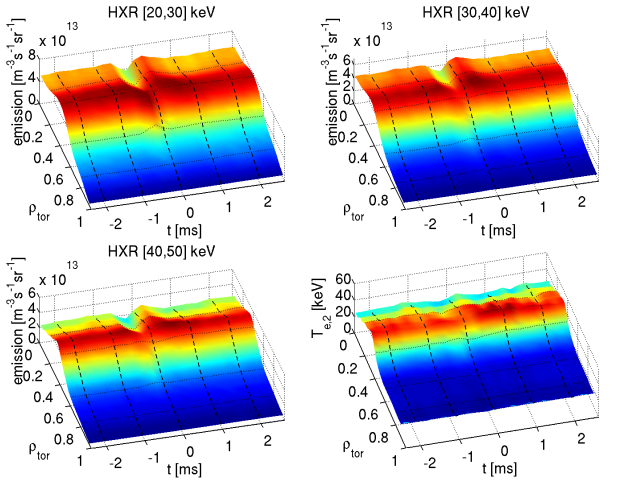

Figure 16. The evolution of radial HXR emission profiles in different energy bins (top left and right and bottom left) and the deduced $T_{e,2}$ profile (bottom right), obtained from HXRS measurements by conditional averaging w.r.t. the start of the p_e rise ($t = 0$) after the last mode-preceding sawtooth crash ($t \approx 0.4\,\mathrm{ms}$); the mode burst occurs in $t = [0.2, 2.2]\,\mathrm{ms}$.

5.5. Discussion

The CAS consist of internal $m/n = 1/1$ kink mode bursts that are coupled to a background $m/n = 2/1$ mode and connected to sawtooth crashes. The bursts have a significant impact on overall confinement and drag the suprathermal electrons around, with a higher radial excursion of the first moment than the thermal electrons. Their excitation can be explained by the coupling to the persistent $m = 2$ component under the flat $q \approx 1$ profile condition after a sawtooth crash, that is predicted by extended MHD theory [48, 50]. The process differs from sawtooth triggering of NTMs [19], where the driving and driven roles are exchanged and the triggered mode is seeded fast (within $100\,\mu\mathrm{s}$) instead of being well separated in time from the sawtooth crash (by $\approx 1\,\mathrm{ms}$). Furthermore, the destabilization of the mode seems to be connected to the faster reheating of the suprathermal electron distribution at the mode location as compared to the thermal e.d.f.. Also, this probably stabilizes the sawtooth [52] until the appearing mode burst reduces confinement and therefore then lowers the sawtooth-destabilizing p_e.

6. Conclusions

The suprathermal electron dynamics during the sawtooth cycle are dominated by the impact of the sawtooth crash and a low and a higher density regime can be distinguished. The intermediate regime can be efficiently studied with the HXRS and exhibits characteristics of both limits. As in the higher density case, the suprathermal electrons show a similar

behavior as the thermal electrons, the slow rise in between crashes is followed by a fast loss of energetic electrons during the crash. This is observable up to energies of 100 keV and the outward transport decreases only marginally with energy in this range. As in the low density case, high energy electrons are transported to the limiter and emit bursts of thick-target bremsstrahlung radiation.
Immediately after the crash, the lower energy part of the suprathermal tail is reheated faster than the thermal and higher energy e.d.f.. Electron acceleration by magnetic reconnection cannot be explicitly observed, but it is conceivable that some electrons are accelerated to runaway energies and undergo such a low number of collisions in the plasma that only their bremsstrahlung emission from the limiting wall can be measured. In this respect, the envisioned implementation of tangential synchrotron radiation measurements for future runaway studies on TCV could even further improve the understanding of electron acceleration in sawtooth crashes.

Although the reliable excitation of the electron fishbone instability on TCV proved more difficult than expected, initial observations and first results could be presented. The significant confinement impact of the fishbone bursts are reflected in a bulk SXR emission drop by $15-25\,\%$. Further development of the scenario is planned and may be aided by recent real-time control upgrades [71].

The effective reheating of the suprathermal tail in its lower energy region seems to play also an important role in the destabilization of the bursty mode. These coupled bursts alternating with sawtooth crashes (CAS) are $m/n = 1/1$ internal kink mode bursts that reduce the central SXR emission (confinement) significantly by up to $15\,\%$. The burst excitation can be explained in connection with coupling to a background $m = 2$ component under the flat $q_{\min} \approx 1$ profile conditions provided by a preceding sawtooth crash.

References

[1] Hofmann F, Lister J B, Anton W, Barry S, Behn R, Bernel S, Besson G, Buhlmann F, Chavan R, Corboz M, Dutch M J, Duval B P, Fasel D, Favre A, Franke S, Heym A, Hirt A, Hollenstein C, Isoz P, Joye B, Llobet X, Magnin J C, Marletaz B, Marmillod P, Martin Y, Mayor J M, Moret J M, Nieswand C, Paris P J, Perez A, Pietrzyk Z A, Pitts R A, Pochelon A, Rage R, Sauter O, Tonetti G, Tran M Q, Troyon F, Ward D J and Weisen H 1994 *Plasma Physics and Controlled Fusion* **36** B277

[2] Coda S 2011 *Nuclear Fusion* **51** 094017

[3] Coda S and Team f t T 2013 *Nuclear Fusion* **53** 104011

[4] Kadomtsev B 1975 *Sov. J. Plasma Phys.* **1** 389–91

[5] Kadomtsev B 1992 *Tokamak Plasma: A Complex Physical System* (Bristol: IOP)

[6] Biskamp D 1993 *Nonlinear Magnetohydrodynamics* (Cambridge: Cambridge University Press)

[7] Sweet P A 1958 The Neutral Point Theory of Solar Flares *Electromagnetic Phenomena in Ionized Gases* p 123

[8] Parker E N 1957 *Phys. Rev.* **107**(3) 830–836

[9] Petschek H 1964 Magnetic Field Annihilation *The Physics of Solar Flares* (Greenbelt, MD) p 425

[10] Kulsrud R M 1998 *Physics of Plasmas* **5** 1599–1606

[11] Kulsrud R M 2001 *Earth Planets Space* **53** 417–422

[12] Porcelli F, Borgogno D, Califano F, Grasso D, Ottaviani M and Pegoraro F 2002 *Plasma Physics and Controlled Fusion* **44** B389

[13] Birn J 2007 *Reconnection of Magnetic Fields* (Cambridge: Cambridge University Press)

[14] Priest E and Forbes T 2000 *Magnetic Reconnection: MHD Theory and Applications* (Cambridge: Cambridge University Press)

[15] Drake J F, Shay M A, Thongthai W and Swisdak M 2005 *Phys. Rev. Lett.* **94** 095001

[16] Webb G M, Axford W I and Terasawa T 1983 *The Astrophysical Journal* **270** 537–553

[17] Shimada N, Terasawa T and Jokipii J 1997 *J. Geophys. Res.* **102** 22301–22310

[18] Tsuneta S and Naito T 1998 *The Astrophysical Journal Letters* **495** L67

[19] Canal G P, Duval B P, Felici F, Goodman T P, Graves J P, Pochelon A, Reimerdes H, Sauter O, Testa D and the Team T 2013 *Nuclear Fusion* **53** 113026

[20] Savrukhin P V 2001 *Phys. Rev. Lett.* **86** 3036–3039

[21] Savrukhin P V 2006 *Plasma Physics and Controlled Fusion* **48** B201

[22] Klimanov I, Fasoli A, Goodman T P and team t T 2007 *Plasma Physics and Controlled Fusion* **49** L1

[23] Imbeaux F and Peysson Y 2000 *Phys. Rev. Lett.* **84**(13) 2873–2876

[24] Pietrzyk Z A, Pochelon A, Goodman T P, Henderson M A, Hogge J P, Reimerdes H, Tran M, Behn R, Furno I, Moret J M, Nieswand C, Rommers J, Sauter O, van Toledo W, Weisen H, Porcelli F and Razumova K A 1999 *Nuclear Fusion* **39** 587

[25] Gnesin S, Coda S, Decker J and Peysson Y 2008 *Review of Scientific Instruments* **79** 10F504 (pages 5)

[26] Kamleitner J, Gnesin S, Coda S, Marmillod P and Decker J 2012 *Europhysics Conference Abstracts* **36F** P1.010

[27] McGuire K, Goldston R, Bell M, Bitter M, Bol K, Brau K, Buchenauer D, Crowley T, Davis S, Dylla F, Eubank H, Fishman H, Fonck R, Grek B, Grimm R, Hawryluk R, Hsuan H, Hulse R, Izzo R, Kaita R, Kaye S, Kugel H, Johnson D, Manickam J, Manos D, Mansfield D, Mazzucato E, McCann R, McCune D, Monticello D, Motley R, Mueller D, Oasa K, Okabayashi M, Owens K, Park W, Reusch M, Sauthoff N, Schmidt G, Sesnic S, Strachan J, Surko C, Slusher R, Takahashi H, Tenney F, Thomas P, Towner H, Valley J and White R 1983 *Phys. Rev. Lett.* **50**(12) 891–895

[28] Nave M F F, Campbell D J, Joffrin E, Marcus F B, Sadler G, Smeulders P and Thomsen K 1991 *Nuclear Fusion* **31** 697

[29] Chen W, Ding X T, Liu Y, Yang Q W, Ji X Q, Isobe M, Yuan G L, Zhang Y P, Zhou Y, Song X Y, Dong Y B, Li W, Zhou J, Lei G J, Cao J Y, Deng W, Song X M, Duan X R and Team H A 2010 *Nuclear Fusion* **50** 084008

[30] von Thun C P, Salmi A, Perona A, Sharapov S E, Pinches S D, Popovichev S, Conroy S, Kiptily V G, Brix M, Cecconello M, Johnson T and Contributors J E 2012 *Nuclear Fusion* **52** 094010

[31] Chen L, White R B and Rosenbluth M N 1984 *Phys. Rev. Lett.* **52**(13) 1122–1125

[32] Coppi B and Porcelli F 1986 *Phys. Rev. Lett.* **57**(18) 2272–2275

[33] Wong K L, Chu M S, Luce T C, Petty C C, Politzer P A, Prater R, Chen L, Harvey R W, Austin M E, Johnson L C, La Haye R J and Snider R T 2000 *Phys. Rev. Lett.* **85**(5) 996–999

[34] Ding X T, Liu Y, Guo G C, Wang E Y, Wong K L, Yan L W, Dong J Q, Cao J Y, Zhou Y, Rao J, Yuan Y, Xia H, Liu Y and group t H M 2002 *Nuclear Fusion* **42** 491

[35] Cesario R, Panaccione L, Marinucci M, Smeulders P, Botrugno A, Calabro G, Castaldo C, Romano A, Pericoli V, Tuccillo A A and Zonca F 2008 Fishbone-like internal kink instability driven by supra-thermal electrons on FTU generated by lower hybrid radiofrequency power (IAEA)

[36] Chen W, Ding X T, Liu Y, Yuan G L, Zhang Y P, Dong Y B, Song X Y, Zhou J, Song X M, Deng W, Yang Q W, Ji X Q, Duan X R, Liu Y and Team t H A 2009 *Nuclear Fusion* **49** 075022

[37] Zhang Y P, Liu Y, Song X Y, Yuan G L, Chen W, Ji X Q, Ding X T, Yang J W, Zhou J, Li X, Yang Q W, Duan X R, Pan C H and Liu Y 2010 *Review of Scientific Instruments* **81** 103501

[38] Macor A, Goniche M, Artaud J F, Decker J, Elbeze D, Garbet X, Giruzzi G, Hoang G T, Maget P, Mazon D, Molina D, Nguyen C, Peysson Y, Sabot R and Ségui J L 2009 *Phys. Rev. Lett.* **102**(15) 155005

[39] Saoutic B, Chatelier M and De Michelis C 2009 *Fusion Science and Technology* **56** 1079–1091

[40] Guimarães Filho Z O, Benkadda S, Elbeze D, Botrugno A, Buratti P, Calabrò G, Decker J, Dubuit N, Garbet X, Maget P, Merle A, Pucella G, Sabot R, Tuccillo A A and Zonca F 2012 *Nuclear Fusion* **52** 094009

[41] Delgado-Aparicio L, Shiraiwa S, Sugiyama L, Parker R, Baek S G, Mumgaard R, Granetz R, Faust I, Scott S, Gates D A, Gorelenkov N, Bertelli N, Bitter M, Gao C, Greenwald M, Hill K, Hubbard A, Hughes J, Irby J, Marmar E, Meneghini O, Pablant N, Phillips P, Rice J E, Rowan W, Walk J, G W, Wilson R, Wolfe S and Wukitch S 2013 *Europhysics Conference Abstracts* **37D** P1.159

[42] Graves J P 2013 *Plasma Physics and Controlled Fusion* **55** 074009

[43] Zonca F, Buratti P, Cardinali A, Chen L, Dong J Q, Long Y X, Milovanov A V, Romanelli F, Smeulders P, Wang L, Wang Z T, Castaldo C, Cesario R, Giovannozzi E, Marinucci M and Ridolfini V P 2007 *Nuclear Fusion* **47** 1588

[44] Vlad G, Briguglio S, Fogaccia G, Zonca F, Fusco V and Wang X 2013 *Nuclear Fusion* **53** 083008

[45] Sangaroon S, Cecconello M, Weiszflog M, Conroy S, Ericsson G, Wodniak I, Keeling D, Turnyanskiy M R and team M 2013 *Europhysics Conference Abstracts* **37D** P5.124

[46] Merle A, Decker J, Garbet X, Sabot R, Guimarães Filho Z O and Nicolas T 2012 *Physics of Plasmas* **19** 072504 (pages 11)

[47] Hender T C, Wesley J C, Bialek J, Bondeson A, Boozer A H, Buttery R J, Garofalo A, Goodman T P, Granetz R S, Gribov Y, Gruber O, Gryaznevich M, Giruzzi G, Günter S, Hayashi N, Helander P, Hegna C C, Howell D F, Humphreys D A, Huysmans G T A, Hyatt A W, Isayama A, Jardin S C, Kawano Y, Kellman A, Kessel C, Koslowski H R, Haye R J L, Lazzaro E, Liu Y Q, Lukash V, Manickam J, Medvedev S, Mertens V, Mirnov S V, Nakamura Y, Navratil G, Okabayashi M, Ozeki T, Paccagnella R, Pautasso G, Porcelli F, Pustovitov V D, Riccardo V, Sato M, Sauter O, Schaffer M J, Shimada M, Sonato P, Strait E J, Sugihara M, Takechi M, Turnbull A D, Westerhof E, Whyte D G, Yoshino R, Zohm H, the ITPA MHD D and Group M C T 2007 *Nuclear Fusion* **47** S128

[48] Brunetti D, Graves J P, Cooper W A and Wahlberg C 2014 *Plasma Physics and Controlled Fusion* **56** 075025

[49] Charlton L A, Hastie R J and Hender T C 1989 *Physics of Fluids B: Plasma Physics (1989-1993)* **1** 798–803

[50] Brunetti D, Graves J P, Halpern F D, Luciani J F, Lütjens H and Cooper W A *Plasma Physics and Controlled Fusion* Accepted for publication

[51] Paley J I, Coda S, Duval B P, Felici F and Moret J M 2010 Architecture and commissioning of the TCV distributed feedback control system *Real Time Conference (RT), 2010 17th IEEE-NPSS* pp 1–6

[52] Goodman T P, Felici F, Sauter O and Graves J P (the TCV Team) 2011 *Phys. Rev. Lett.* **106**(24) 245002

[53] Kamleitner J, Coda S, Decker J, Graves J P and Gnesin S 2013 *Europhysics Conference Abstracts* **37D** P5.127

[54] Kamleitner J, Coda S and Decker J 2014 Suprathermal electron dynamics and hard X-ray tomography in TCV *56th Annual Meeting of the APS Division of Plasma Physics* vol 49 p TP8.43

[55] Sushkov A, Andreev V, Camenen Y, Pochelon A, Klimanov I, Scarabosio A and Weisen H 2008 *Review of Scientific Instruments* **79** 023506 (pages 5)

[56] Anton M, Dutch M J and Weisen H 1995 *Review of Scientific Instruments* **66** 3762–3769

[57] Anton M, Weisen H, Dutch M J, von der Linden W, Buhlmann F, Chavan R, Marlétaz B, Marmillod P and Paris P 1996 *Plasma Physics and Controlled Fusion* **38** 1849

[58] Kamleitner J 2011 General tomographic inversion at TCV Tech. rep. CRPP, EPFL

[59] Furno I, Angioni C, Porcelli F, Weisen H, Behn R, Goodman T, Henderson M, Pietrzyk Z, Pochelon A, Reimerdes H and Rossi E 2001 *Nuclear Fusion* **41** 403

[60] Furno I, Weisen H and team t T (TCV team) 2003 *Physics of Plasmas* **10** 2422–2428

[61] Furno I, Weisen H, Carey C, Angioni C, Behn R, Fable E, Zabolotsky A, team t T and Contributors J E 2005 *Plasma Physics and Controlled Fusion* **47** 49

[62] Moret J M, Buhlmann F, Fasel D, Hofmann F and Tonetti G 1998 *Review of Scientific Instruments* **69** 2333–2348

[63] Savrukhin P V 2002 *Review of Scientific Instruments* **73** 4243–4245

[64] Savrukhin P V and Klimanov I 2001 *Review of Scientific Instruments* **72** 1668–1671

[65] Gnesin S 2011 *Electron Cyclotron Heating and Suprathermal Electron Dynamics in the TCV Tokamak* Ph.D. thesis EPFL

[66] Kamleitner J, Coda S, Gnesin S and Marmillod P 2014 *Nuclear Instruments and Methods in Physics Research Section A: Accelerators, Spectrometers, Detectors and Associated Equipment* **736** 88–98 ISSN 0168-9002

[67] Klimanov I, Porte L, Alberti S, Blanchard P, Fasoli A and Goodman T P 2005 *Review of Scientific Instruments* **76** 093504 (pages 6)

[68] Behn R, Rommers J H, Pitts R A, Pietrzyk Z A, Chavan R and Marletaz B 1999 *Review of Scientific Instruments* **70** 768–771

[69] Zhuang G, Behn R, Klimanov I, Nikkola P and Sauter O 2005 *Plasma Physics and Controlled Fusion* **47** 1539

[70] Barry S, Nieswand C and Prunty S L 1997 *Proceedings of the 8th International Symposium on Laser-aided Plasma Diagnostics* 313–318

[71] Felici F, Goodman T P, Sauter O, Canal G, Coda S, Duval B P, Rossel J X and the Team T 2012 *Nuclear Fusion* **52** 074001